

# Nanoscale

Accepted Manuscript



This is an *Accepted Manuscript*, which has been through the Royal Society of Chemistry peer review process and has been accepted for publication.

*Accepted Manuscripts* are published online shortly after acceptance, before technical editing, formatting and proof reading. Using this free service, authors can make their results available to the community, in citable form, before we publish the edited article. We will replace this *Accepted Manuscript* with the edited and formatted *Advance Article* as soon as it is available.

You can find more information about *Accepted Manuscripts* in the [Information for Authors](#).

Please note that technical editing may introduce minor changes to the text and/or graphics, which may alter content. The journal's standard [Terms & Conditions](#) and the [Ethical guidelines](#) still apply. In no event shall the Royal Society of Chemistry be held responsible for any errors or omissions in this *Accepted Manuscript* or any consequences arising from the use of any information it contains.

## COMMUNICATION

## Preparation of porous Sn@C nanocomposite as high-performance anode material for lithium-ion batteries

Cite this: DOI: 10.1039/x0xx00000x

YanJun Zhang, Li Jiang and Chunru Wang\*

Received 00th January 2015,  
Accepted 00th January 2015

DOI: 10.1039/x0xx00000x

www.rsc.org/

**Porous Sn@C nanocomposite was prepared via a facile hydrothermal method combined with a simple post-calcination process, using stannous octoate as Sn sources and glucose as C sources. The as-prepared Sn@C nanocomposite exhibited excellent electrochemical behavior with high reversible capacity, long cycle life and good rate capability when used as anode material for lithium ion batteries.**

Rechargeable lithium-ion batteries (LIBs) have been widely used in many portable electronic devices during the past few years, and being expected to apply in future electric vehicles and the renewable energy storage. To meet the requirement for LIBs with high energy density, long cycle life, excellent rate capability performance, and environmental compatibility, extensive efforts have been made to develop new electrode materials and to design new structures of electrode materials.<sup>1-3</sup> For anode materials, the already-commercialized graphite is far from meeting the demand for high energy and power density because of its low theoretical capacity ( $372 \text{ mAh g}^{-1}$ ).<sup>4,5</sup> Therefore, many efforts have been devoted to developing new anode materials, such as Si-based materials,<sup>6-8</sup> metal alloys,<sup>9-11</sup> transition metal oxides (TMOs)<sup>12-14</sup> and layered metal chalcogenides.<sup>15-17</sup> Among them, metallic tin (Sn), has been considered as one of the most promising alternative anode materials for next generation LIBs, due to its high theoretical specific capacity ( $\text{Li}_{4.4}\text{Sn}$ ,  $992 \text{ mAh g}^{-1}$ ) and an appropriate low discharge potential versus  $\text{Li}/\text{Li}^+$ .<sup>18-20</sup> However, the practical application of Sn has been greatly hampered by its pulverization problem caused by the huge volume change during lithiation/delithiation processes, leading to a loss in contact with the current collector, and consequently a rapid capacity fading in the cycling.<sup>21, 22</sup>

Up to now, enormous efforts have been made to improve the electrochemical performance of Sn as anode material for LIBs.<sup>23-28</sup> One of the most successful methods for improving the cycling stability is to form a Sn@C nanocomposite by dispersing Sn

nanoparticles into a porous carbon matrix.<sup>28-43</sup> The porous structures provide additional space to accommodate the volume change, reducing the pulverization of Sn. The porous carbon matrix can also avoid the aggregation of Sn nanoparticles, provide a continuous electron pathway and allow  $\text{Li}^+$  access. To date, a few porous Sn@C nanocomposites have been obtained by electrospinning technique,<sup>29-32</sup> aerosol spray pyrolysis process,<sup>33, 34</sup> and other methods.<sup>35-43</sup> These porous Sn@C nanocomposites show improved electrochemical performances as anode materials for LIBs compared with bare Sn. However, the preparation of porous Sn@C nanocomposites reported previously involves complicated processes.

In this paper, we report a facile hydrothermal method combined with a simple post-calcination process for the preparation of porous Sn@C nanocomposite, using stannous octoate as Sn sources and glucose as C sources. The as-prepared porous Sn@C nanocomposite exhibited excellent electrochemical behavior with high reversible capacity, long cycle life and high rate capability when used as anode material for LIBs.

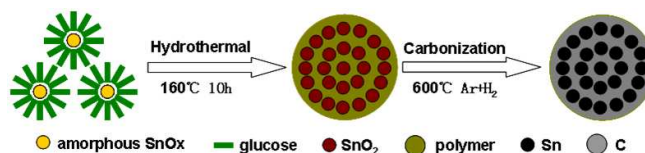


**Fig. 1** Schematic illustration of the preparation process of the porous Sn@C nanocomposite.

Porous Sn@C nanocomposite was successfully prepared via a facile hydrothermal method combined with a simple post-calcination process, as shown in Fig. 1. Details for the preparation of porous Sn@C nanocomposite are presented in the Supporting Informations (ESI). Due to the unstable properties of stannous octoate, the amorphous  $\text{SnO}_x$  nanoparticles were first produced when stannous octoate was added to the glucose solution. The TEM image and XRD pattern of the amorphous  $\text{SnO}_x$  nanoparticles are shown in ESI (Fig. S1). After hydrothermal treatment, spherical  $\text{SnO}_2$ @polymer

nanocomposite was obtained with the ultrasmall SnO<sub>2</sub> nanoparticles dispersed in the polymer spheres formed by dehydration and polymerization of the glucose.<sup>38</sup> During the subsequently carbonization process, the SnO<sub>2</sub> nanoparticles were in situ reduced to Sn nanoparticles along with the carbonization of polymer yields the porous Sn@C nanocomposite.

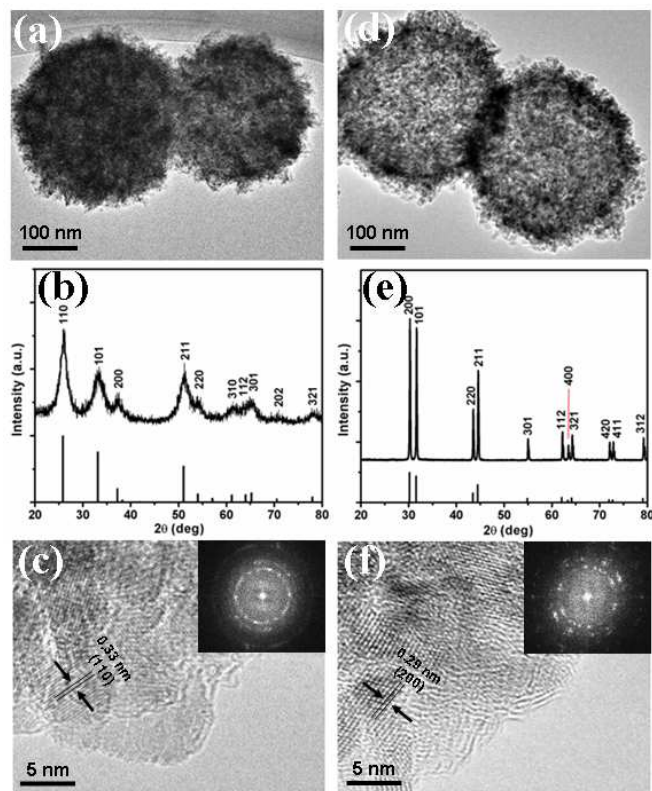


**Fig. 2** (a) TEM image, (b) XRD pattern, and (c) HRTEM image (inset is the corresponding FFT pattern) of the as-obtained precipitate after hydrothermal treatment. (d) TEM image, (e) XRD pattern, and (f) HRTEM image (inset is the corresponding FFT pattern) of the porous Sn@C nanocomposite.

The morphologies of the samples were characterized using scanning electron microscopy (SEM) and transmission electron microscopy (TEM). It is clear from the SEM images (Fig. S2a) that the precipitate obtained after hydrothermal treatment exhibits spherical nanostructures with rough surface, and the diameters range from 100 to 300 nm. Fig. 2a depicts a typical TEM image of the precipitate obtained after hydrothermal treatment. Ultrasmall SnO<sub>2</sub> nanoparticles (black dots) were homogeneously embedded in the polymer sphere. Fig. 2b shows the XRD pattern of the as-obtained precipitate after hydrothermal treatment. All the diffraction peaks in the XRD pattern can be indexed to the rutile-phase SnO<sub>2</sub> according to the standard XRD data file (JCPDS file No. 41-1445). The detailed structures were confirmed by high-resolution transmission electron microscopy (HRTEM). As shown in Fig. 2c, crystal SnO<sub>2</sub> nanoparticles with size of around 5 nm were wrapped in the polymer. During the carbonization process to prepare Sn@C nanocomposite, the spherical morphology was still maintained, as can be seen from SEM (Fig. S2b) and TEM (Fig. 2d) images. The porous structure of the spherical Sn@C nanocomposite can be also confirmed from Fig. 2d. It is believed that the porous structure was

result from the decomposition of polymer with gases releasing during the carbonization process. The XRD pattern shown in Fig. 2e substantiates the complete reduction from SnO<sub>2</sub> to metallic Sn. All diffraction peaks can be readily indexed to crystalline Sn (JCPDS file No. 86-2265). The HRTEM image (Fig. 2f) of the porous Sn@C nanocomposite reveals that the crystal Sn nanoparticles with size of around 5 nm were homogeneously embedded in the carbon matrix.

The Raman spectrum of the porous Sn@C nanocomposite was shown in Fig. S3, in which the two broad peaks at 1341 and 1594 cm<sup>-1</sup> can be assigned to typical D and G bands of amorphous carbon, respectively.<sup>44</sup> It is well known that amorphous carbon contains abundant defects and vacancies, which not only favor the diffusion of lithium ions, but also provide more reversible sites for Li storage.<sup>45</sup> The composition analysis of the porous Sn@C nanocomposite was determined by thermogravimetric (TG) analysis (Fig. S4). Considering the full oxidation of Sn to SnO<sub>2</sub> at 800 °C in air, the content of Sn in the nanocomposite is evaluated to be 64.3%. The Brunauer-Emmett-Teller (BET) surface area of the porous Sn@C nanocomposite was measured to be about 240.08 m<sup>2</sup> g<sup>-1</sup> by the N<sub>2</sub> sorption measurement at 77 K (Fig. S5). The adsorption-desorption isotherm with a hysteresis loop in the P/P<sub>0</sub> range of 0.40-0.95, suggesting the existence of micropores and mesopores in the Sn@C nanocomposite. These pores presumably arise from the defects and porous structure in the C layers induced by the gases releasing during the carbonization process.

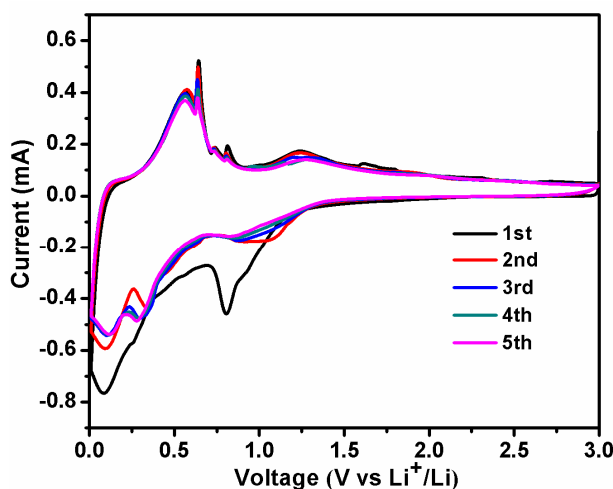


**Fig. 3** Cyclic voltammetry plots of the porous Sn@C nanocomposite electrode at a scan rate of 0.1 mV s<sup>-1</sup> in the voltage range of 0.01-3.0 V versus Li<sup>+</sup>/Li.

The electrochemical performance of the as-prepared porous Sn@C nanocomposite was first evaluated by the cyclic voltammetry. Fig. 3 shows the first five consecutive cyclic voltammograms (CVs) of the electrode made from the porous Sn@C nanocomposite in the voltage range 0.01-3.0 V versus Li/Li<sup>+</sup> at a scan rate of 0.1 mV s<sup>-1</sup>. During the first cathodic scan, the visible peak located at around 0.80 V may be associated with the solid electrolyte interphase (SEI) layer formation and the reduction of SnO<sub>x</sub> on the surface of Sn.<sup>28</sup> The other two reduction peaks located at around 0.10 and 0.27 V may be assigned to the lithiation reaction between Sn and lithium to form the Li<sub>x</sub>Sn alloy. The corresponding oxidation peaks between

0.25 to 0.9 V may be assigned to the delithiation reaction of the  $\text{Li}_x\text{Sn}$  alloy.<sup>42,43</sup> The broad anodic peak at around 1.25 V represents lithium extraction from carbon.<sup>38</sup> The difference between the first and the later cathodic scans is mainly attributed to the decomposition of the electrolyte to form SEI films, corresponding to the capacity loss during the first cycle. All peaks are reproducible and stable after the first cycle, implying the good reversibility of the electrochemical reactions of the porous Sn@C electrode.

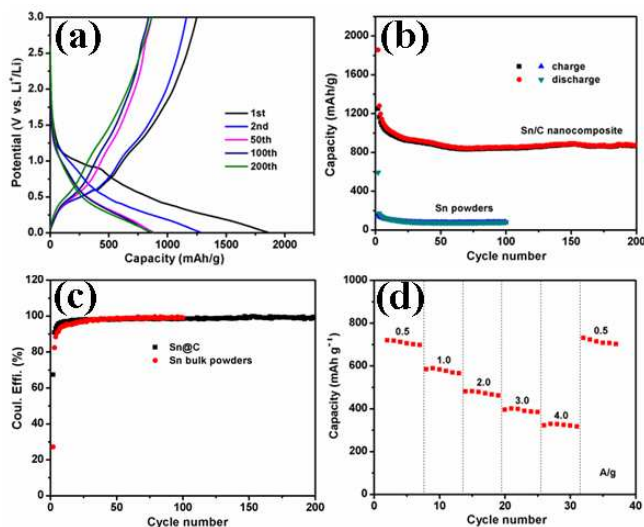


**Fig. 4** (a) The discharge-charge voltage profiles at a current density of 200  $\text{mA g}^{-1}$ . (b) Cycling performances for the electrodes of porous Sn@C nanocomposite and bulk Sn powder in the voltage range of 0.01–3 V (versus  $\text{Li}^+/\text{Li}$ ) at a current density of 200  $\text{mA g}^{-1}$ , and (c) the corresponding Coulombic efficiency. (d) Rate performance of the electrode made from porous Sn@C nanocomposite.

Fig. 4a illustrates the 1st, 2nd, 50th, 100th and 200th discharge-charge voltage profiles of the porous Sn@C nanocomposite as anode materials for rechargeable lithium batteries at a current density of 200  $\text{mA g}^{-1}$ , and the measurement was performed at room temperature in a potential window of 0.01 to 3.0 V (versus  $\text{Li}^+/\text{Li}$ ). The voltage profiles are typical characteristics of the electrochemical process of lithium alloying-dealloying in Sn electrode. In the discharge curves, the slope ranges from 1.0 to 0.01 V can be associated with the lithiation reaction between Sn and lithium to form the  $\text{Li}_x\text{Sn}$  alloy. In the charge curves, the slope ranges from 0.25 to 0.9 V can be associated with the delithiation process of the  $\text{Li}_x\text{Sn}$  alloy. The slope above 1.0 V can be associated with the lithium extraction from porous carbon. This result is in good agreement with the CV curves. All the specific capacity values reported in this paper are calculated on the basis of the total mass of Sn@C nanocomposite. The first discharge and charge delivered a specific capacity of 1855 and 1249  $\text{mAh g}^{-1}$ , respectively. The large initial capacity loss of the porous Sn@C nanocomposite electrode can be partly attributed to the decomposition of the electrolyte that generates a thick SEI layer on the electrode surface and the storage of  $\text{Li}^+$  in porous carbon, which are difficult to extract. The repeatability and slow shrinkage of charge/discharge curves after the first cycle demonstrate the good cycling stability of the as-prepared porous Sn@C nanocomposite electrode.

Fig. 4b displays the discharge-charge capacity versus cycle number for the porous Sn@C nanocomposite at a current density of 200  $\text{mA g}^{-1}$  between 0.01–3 V. For comparison, the cycling behavior of the commercial Sn powders was also evaluated under the same conditions. As can be seen, the porous Sn@C nanocomposite electrode exhibits good capacity retention during 200 discharge/charge cycles. After 200 cycles, it still retains a capacity of 865.3  $\text{mAh g}^{-1}$ , which is 2.3 times higher than that of traditional graphitic anode (372  $\text{mAh g}^{-1}$ ). The capacity fading in the initial several cycles may be derived from the partial irreversible insertion of lithium ions into the porous carbon.<sup>33</sup> In contrast, the commercial Sn powders (Fig. S6) show a very poor lithium storage performance, for which the initial discharge and charge capacities are only 592.4 and 160.4  $\text{mAh g}^{-1}$ , respectively. The capacity of commercial Sn powders retained only 89.3  $\text{mAh g}^{-1}$  after 20 cycles. Obviously, the porous Sn/C nanocomposite electrode has greatly improved cycling performance. Moreover, as can be seen from the Fig. 4c, the porous Sn@C nanocomposite electrode displays an initial Coulombic efficiency (CE) of 67.3%, which is higher than that of the commercial Sn powders electrode (27.1%). The high CE of >95% was achieved after several cycles, demonstrating high reversibility of the porous Sn@C nanocomposite electrode. When compared with other previously reported Sn anode materials, our porous Sn@C nanocomposite exhibits higher capacity and longer cycle life than most samples at similar rates. The superior cycling performance may be attributed to the following several merits of the porous Sn@C nanocomposite. First, the ultrasmall size of Sn nanoparticles, which can significantly reduce the strain generated during the lithiation/delithiation processes and improve the electrochemical performance of electrode materials.<sup>29–32</sup> Second, the porous carbon matrix, which can not only prevent Sn nanoparticles aggregation over repeated cycling, but also render sufficient void space to accommodate the large volume change of Sn nanoparticles, thus maintaining the structural integrity and electrical conductivity of the electrode.<sup>33–37</sup> Third, the homogeneous distribution of Sn nanoparticles in the porous carbon matrix, which generate a balanced stress over the whole composite and the electrode, and thus preventing local cracking of the electrode.<sup>38–40</sup> Finally, the large specific surface area ensures a high electrode/electrolyte contact area, which can significantly improve the transport for electrons and lithium ions, thus decreasing polarization and increasing capacity.<sup>41–43</sup> These merits make as-prepared Sn@C nanocomposite a very promising anode material for LIBs.

Excellent rate property is another indispensable capability for electrodes as advanced LIBs. Thus, the rate property of the porous Sn@C nanocomposite was characterized at various current densities and is shown in Fig. 4d. As the current density changed from 0.5 to 4.0  $\text{A g}^{-1}$ , the specific reversible capacity of the sample falls moderately with increasing current density. The corresponding discharge-charge profiles are given in Supporting Information Fig. S7. As the current density was reduced to low current, the capacity also recovered completely. The result indicates that the structure of porous Sn@C nanocomposite is stable at various current densities. The excellent rate property should be result from the combined advantages of ultrasmall Sn nanoparticles and porous carbon matrix, as well as the unique feature of the sphere geometries.

Moreover, the morphology and structure changes of the porous Sn@C nanocomposite after 200 charge-discharge cycles at 200 mA g<sup>-1</sup> were investigated using TEM. It is clearly seen from the TEM image (Fig. S8) that the Sn@C nanocomposite still maintained the spherical shape even after long time cycling. Sn nanoparticles were still homogeneously embedded in the carbon matrix. This further certifies that the unique structure of porous Sn@C nanocomposite effectively alleviates the pulverization and prevents the particle aggregation, guaranteeing efficient electrochemical performance.

In conclusion, porous Sn@C nanocomposite was successfully prepared via a facile hydrothermal method combined with a simple post-calcination process. Ultrasmall Sn nanoparticles were homogeneously distributed in a spherical porous carbon matrix. The as-prepared porous Sn@C nanocomposite showed a reversible capacity of 865.3 mAh g<sup>-1</sup> after 200 discharge/charge cycles at a current density of 200 mA g<sup>-1</sup>. Moreover, the porous Sn@C nanocomposite exhibited excellent rate capability as the current density changed from 0.5 to 4.0 A g<sup>-1</sup>. It is believed that the superior electrochemical performance of the porous Sn@C nanocomposite should be result from the combined merits of ultrasmall Sn nanoparticles and porous carbon matrix, as well as the unique feature of the sphere geometries. The high specific capacity, long stability and outstanding rate property make the porous Sn@C nanocomposite a promising anode material for advanced LIBs.

## Acknowledgements

This work is supported by the National Basic Research Program (No.2012CB932900), the National Basic Research Program (No. 2011CB933700), the National Key Technology Support Program (No.2012BAJ25B08) and the National Natural Science Foundation of China (No. 21121063, 11179006, 20903107).

## Notes and references

Key Laboratory of Molecular Nanostructure and Nanotechnology, Beijing National Laboratory for Molecular Sciences, Institute of Chemistry, Chinese Academy of Sciences, Beijing 100190, E-mail: crwang@iccas.ac.cn.

Electronic Supplementary Information (ESI) available: Detailed experimental procedure, additional Raman spectra, TGA curve, N<sub>2</sub> adsorption-desorption isotherms and SEM images. See DOI: 10.1039/c000000x/

- 1 Y. G. Guo, J. S. Hu and L. J. Wan, *Adv. Mater.*, 2008, **20**, 4384.
- 2 P. G. Bruce, B. Scrosati and J. M. Tarascon, *Angew. Chem. Int. Ed.*, 2008, **47**, 2930.
- 3 Y. Liang, R. Feng, S. Yang, H. Ma, J. Liang and J. Chen, *Adv. Mater.*, 2011, **23**, 640.
- 4 Y. Idota, T. Kubota, A. Matsufuji, Y. Maekawa, T. Miyasaka, *Science*, 1997, **276**, 1395.
- 5 M. H. Park, M. G. Kim, J. Joo, K. Kim, J. Kim, S. Ahn, Y. Cui, J. Cho, *Nano Lett.*, 2009, **9**, 3844.
- 6 H. Kim, M. Seo, M. H. Park, J. Cho, *Angew. Chem. Int. Ed.*, 2010, **49**, 2146.
- 7 L. F. Cui, R. Ruffo, C. K. Chan, H. Peng, Y. Cui, *Nano Lett.*, 2009, **9**, 491.
- 8 X. Fan, H. Zhang, N. Du, P. Wu, X. Xu, Y. Li, D. Yang, *Nanoscale*, 2012, **4**, 5343.
- 9 C. M. Park, J. H. Kim, H. Kim, H. J. Sohn, *Chem. Soc. Rev.*, 2010, **39**, 3115.

- 10 J. X. Zhu, T. Sun, J. S. Chen, W. H. Shi, X. J. Zhang, X. W. Lou, S. Mhaisalkar, H. H. Hng, F. Boey, J. Ma, Q. Y. Yan, *Chem. Mater.*, 2010, **22**, 5333.
- 11 Z. Wang, M. Gu, Y. Zhou, X. Zu, J. G. Connell, J. Xiao, D. Perea, L. J. Lauhon, J. Bang, S. Zhang, C. Wang, F. Gao, *Nano Lett.*, 2013, **13**, 4511.
- 12 M. V. Reddy, G. V. S. Bao, B. V. R. Chowdari, *Chem. Rev.*, 2013, **113**, 5364.
- 13 J. A. Jiang, Y. Y. Li, J. P. Liu, X. T. Huang, *Nanoscale*, 2011, **3**, 45.
- 14 S. H. Choi, J. H. Lee, Y. C. Kang, *Nanoscale*, 2013, **5**, 12645.
- 15 K. Shiva, H. S. S. R. Matte, H. B. Rajendra, A. J. Bhattacharyya, C. N. R. Rao, *Nano Energy*, 2013, **2**, 787.
- 16 J. M. Jeong, K. G. Lee, S. J. Chang, J. W. Kim, Y. K. Han, S. J. Lee, B. G. Choi, *Nanoscale*, 2015, **7**, 324.
- 17 H. J. Yoo, A. P. Tiwari, J. T. Lee, D. Kim, J. H. Park, H. Lee, *Nanoscale*, 2015, **7**, 3404.
- 18 R. Z. Hu, Q. Shi, H. Wang, M. Q. Zeng, M. Zhu, *J. Phys. Chem. C*, 2009, **113**, 18953.
- 19 M. G. Kim, S. Sim, J. Cho, *Adv. Mater.*, 2010, **22**, 5154.
- 20 Y. Q. Zou, Y. Wang, *ACS Nano*, 2011, **5**, 8108.
- 21 Q. Mao, R. A. Dunlap, J. R. Dahn, *J. Electrochem. Soc.*, 1999, **146**, 405.
- 22 L. W. Ji, Z. K. Tan, T. Kuykendall, E. J. An, Y. B. Fu, V. Battaglia, Y. G. Zhang, *Energy Environ. Sci.*, 2011, **4**, 3611.
- 23 G. Derrien, J. Hassoun, S. Panero, B. Scrosati, *Adv. Mater.*, 2007, **19**, 2336.
- 24 C. D. Wang, Y. Li, Y. S. Chui, Q. H. Wu, X. F. Chen, W. J. Zhang, *Nanoscale*, 2013, **5**, 10599.
- 25 K. Kravchyk, L. Protesescu, M. L. Bodnarchuk, F. Krumeich, M. Yarema, M. Walter, C. Guntlin, M. V. Kovalenko, *J. Am. Chem. Soc.*, 2013, **135**, 4199.
- 26 Z. J. Li, W. Lv, C. Zhang, J. W. Qin, W. Wei, J. J. Shao, D. W. Wang, B. H. Li, F. Y. Kang, Q. H. Yang, *Nanoscale*, 2014, **6**, 9554.
- 27 J. Qin, C. N. He, N. Q. Zhao, Z. Y. Wang, C. S. Shi, E. Z. Liu, J. J. Li, *ACS nano*, 2014, **8**, 1728.
- 28 X. K. Huang, S. M. Cui, J. B. Chang, P. B. Hallac, C. R. Fell, Y. T. Luo, B. Metz, J. W. Jiang, P. T. Hurley, J. H. Chen, *Angew. Chem. Int. Ed.*, 2015, **54**, 1490.
- 29 Y. Yu, L. Gu, C. Zhu, P. A. Aken, J. Maier, *J. Am. Chem. Soc.*, 2009, **131**, 15984.
- 30 Y. Yu, L. Gu, C. Wang, A. Dhanabalan, P. A. Aken, J. Maier, *Angew. Chem. Int. Ed.*, 2009, **48**, 6485.
- 31 Y. Yu, Q. Yang, D. Teng, X. Yang, S. Ryu, *Electro. Commun.*, 2010, **12**, 1187.
- 32 I. Meschini, F. Nobili, M. Mancini, R. Marassi, R. Tossici, A. Savoini, M. L. Focarete, F. Croce, *J. Power Sources*, 2013, **226**, 241.
- 33 Y. H. Xu, Q. Liu, Y. J. Zhu, Y. H. Liu, A. Langrock, M. R. Zachariah, C. S. Wang, *Nano Lett.*, 2013, **13**, 470.
- 34 N. Zhang, Q. Zhao, X. P. Han, J. G. Yang, J. Chen, *Nanoscale*, 2014, **6**, 2827.
- 35 K. T. Lee, Y. S. Jung, S. M. Oh, *J. Am. Chem. Soc.*, 2003, **125**, 5652.
- 36 G. Derrien, J. Hassoun, S. Panero, B. Scrosati, *Adv. Mater.*, 2007, **19**, 2336.
- 37 G. Cui, Y. S. Hu, L. Zhi, D. Wu, I. Lieberwirth, J. Maier, K. Müllen, *Small*, 2007, **3**, 2066.
- 38 W. M. Zhang, J. S. Hu, Y. G. Guo, S. F. Zheng, L. S. Zhong, W. G. Song, L. J. Wan, *Adv. Mater.*, 2008, **20**, 1160.
- 39 Y. Qiu, K. Yan, S. Yang, *Chem. Commun.*, 2010, **46**, 8359.
- 40 J. Chen, L. Yang, S. Fang, S. Hirano, *Electro. Commun.*, 2011, **13**, 848.
- 41 Y. H. Xu, J. C. Guo, C. S. Wang, *J. Mater. Chem.*, 2012, **22**, 9562.
- 42 Y. H. Xu, Y. J. Zhu, Y. H. Liu, C. S. Wang, *Adv. Energy Mater.*, 2013, **3**, 128.
- 43 Z. Q. Zhu, S. W. Wang, J. Du, Q. Jin, T. R. Zhang, F. Y. Cheng, J. Chen, *Nano Lett.*, 2014, **14**, 153.
- 44 J. Hwang, S. H. Woo, J. Shim, C. Jo, K. T. Lee, J. Lee, *ACS Nano*, 2013, **7**, 1036.
- 45 T. Zheng, Q. Zhong, J. R. Dahn, *J. Electrochem. Soc.*, 1995, **142**, L211.